

Electron and Hole Intraband Spectroscopy of GaSe Nanoparticles

H. Tu,[†] V. Chikan,[‡] and D. F. Kelley^{*,†}

Department of Chemistry, Kansas State University, Manhattan, Kansas 66506-3701

Received: February 4, 2003; In Final Form: May 20, 2003

The electron and hole intraband spectroscopy in GaSe nanoparticles having diameters ranging from 4 to 9 nm is studied by femtosecond transient absorption polarization methods. The results indicate that the transient absorption spectrum in the 500–700 nm region has a size-independent peak at about 600 nm. Polarization results indicate that the absorption anisotropy is small or negative on the blue edge of the spectrum and increases with increasing wavelength. The anisotropy reaches a maximum in the 600 nm region and remains approximately constant out to 700 nm. Smaller particles exhibit smaller (or more negative) anisotropies and a larger wavelength dependence than larger particles. These results are interpreted in terms of a simple effective mass model. Due to the approximately cylindrical symmetry of these two-dimensional particles, the electron and hole states are described by particle-in-a-cylinder wave functions and the optical transitions may be calculated from these wave functions. These calculations semiquantitatively predict the absorption maximum at 600 nm and qualitatively predict the wavelength dependence of the absorption polarization. They are also consistent with the size dependence of the anisotropy spectrum. Absorption near the 600 nm maximum is assigned to an out-of-plane hole intraband transition, while the transient absorptions to the blue of the maximum are assigned to in-plane electron and hole intraband transitions. The observation of a positive anisotropy at the longest wavelengths suggests the presence of a weak underlying, *z*-polarized electron intraband transition at redder wavelengths. These assignments are consistent with the previously reported studies indicating that the absorption is largely quenched in the presence of the hole acceptor, pyridine.

Introduction

The spectroscopy and charge carrier dynamics in semiconductor nanoparticles have received increasing attention in recent years. The properties of the charge carriers, electrons and holes, along with their spectroscopy have been extensively studied. It is largely these properties that determine the technological applications for which any type of semiconductor nanoparticle is well suited.¹ The rates of carrier relaxation and trapping as well as the dynamics of interfacial charge transfer are of particular interest. One of the most unambiguous ways to elucidate these dynamics is through the spectroscopy of electron and hole intraband transitions. Electron intraband transitions have been extensively studied in CdSe^{2–7} and, to a lesser extent, InP nanoparticles.⁸

Charge carrier dynamics have been studied in several different types of semiconductor nanoparticles. The nanoparticles in which carrier trapping rates have been studied include CdS,^{9–12} InP,^{13–15} PbSe,¹⁶ SnO,¹⁷ and several others.^{18–20} There is often a high density of surface trap states, and electron and hole trapping occurs rapidly, in less than a few picoseconds. The carrier trapping dynamics in MoS₂ and related types of nanoparticles have also been studied.^{21,22} In these cases, the combination of time-resolved absorption and emission polarization spectroscopies along with carrier quencher and injection studies allow the electron and hole dynamics to be separated.^{23–26} Due to well-developed synthetic methods, the most thoroughly

studied type of nanoparticle is CdSe. In this case, the electron intraband spectroscopy as well as relaxation rates have been extensively studied. The results show that electron relaxation is facilitated by Auger interactions with the hole and occurs on the subpicosecond time scale.^{6,7,27,28} However, in the absence of the hole and therefore electron–hole Auger processes, much slower relaxation (picoseconds to hundreds of picoseconds) is observed.^{28,29} Subsequent electron and hole trapping processes have also been studied and occur on longer time scales.^{5,29,30} Carrier quenching and time-resolved emission results complement transient absorption studies and have permitted assignment of the observed transients to electron or hole processes. The results indicate the trapping of holes into shallow, intrinsic surface states occurs on the 2 ps time scale, while electron trapping into surface defect states occurs on the 30 ps time scale. These processes are followed by subsequent relaxation to deeper trap states.⁵

GaSe has very interesting and somewhat unusual structural and electronic properties. Our initial studies indicate that much of the GaSe nanoparticle spectroscopy can be understood in terms of these properties.^{31–33} GaSe has a hexagonal layered structure consisting of Se–Ga–Ga–Se tetralayered sheets.³⁴ Each of the two selenium sheets consists of a two-dimensional hexagonally close-packed plane of selenium atoms, with the selenium atoms in each of the planes aligned with those in the opposing plane. The gallium atoms are in pairs, aligned along the *z* axis (perpendicular to the selenium planes) in the trigonal prismatic sites between the selenium sheets. Bulk GaSe consists of Se–Ga–Ga–Se tetralayer sheets, separated by a relatively large gap, and having only weak, primarily van der Waals interactions holding the Se–Ga–Ga–Se tetralayer sheets to

* To whom correspondence should be addressed: e-mail dfkelley@ucmerced.edu.

[†] Address after July 1, 2003: University of California—Merced, Merced, CA 95344.

[‡] Present address: Division of Chemical Sciences, Lawrence Berkeley National Laboratory, 1 Cyclotron Road, Mail Stop 2R0300, Berkeley, CA 94720.

each other. There are three different crystal structures of GaSe (β , γ , and ϵ), differing in how the Se–Ga–Ga–Se layers stack on each other. A single tetralayer is basically a two-dimensional structure, having the point group D_{3h} .¹ The simplest three-dimensional structure is the β -polytype, having the point group D_{6h} .⁴

Bulk GaSe is a photoluminescent, indirect band gap semiconductor, having a 2.11 eV direct band gap^{35,36} and an indirect transition at a slightly lower (25 meV) energy. In high-quality crystals, emission is seen almost entirely from the direct band-edge exciton.^{37,38} Depending on the defect density of the crystal, emission may also be observed from the indirect band-edge exciton and from trap states. The lowest allowed transition is at Γ and, in the absence of spin–orbit coupling, is polarized perpendicular to the selenium and gallium planes (z -polarized). At a somewhat higher energy (about 0.5 eV) there is an x,y -polarized absorption, corresponding to a transition from lower in the valence band to the bottom of the conduction band at Γ . Spin–orbit coupling mixes these transitions, slightly reducing the extent to which they are polarized.

We have very recently synthesized and characterized GaSe nanoparticles.³¹ We have noticed that in many solvents these nanoparticles are quite photostable. This may be understood in terms of the electronic structure of the bulk material. Excitation of the direct band gap transition results in an electronic nodal plane between the layers of gallium atoms.^{35–37} Production of a node in the electronic wave function at the plane midway between the planes of gallium atoms corresponds to considerable Ga–Ga, σ^* character in the band-edge states, which does little to weaken the Ga–Se bonds. This is in contrast to many other types of semiconductor nanoparticles that have considerable metal–chalcogenide σ^* character in the excited states. Hence, GaSe is expected to be more photostable than many other types of semiconductor nanoparticles.

The synthesis used to obtain GaSe nanoparticles is similar to that used to obtain CdSe nanoparticles.³⁹ This single-injection synthesis results in particles having diameters between 2 and 6 nm. Subsequent chromatographic separation results in samples of smaller particles, averaging about 2.5 nm in diameter. Larger particles may be produced by multiple injections of the precursors, as described below. Electron diffraction results indicate that in all cases the particles are disks, exactly four atoms thick; that is, they have a single tetralayer (Se–Ga–Ga–Se) morphology. These particles have edges that are capped with trioctyl phosphine (TOP) and/or trioctyl phosphine oxide (TOPO). GaSe nanoparticles are strongly luminescent with an emission quantum yield of about 15%. Time-resolved emission studies on 4 nm particles have shown that, following 400 nm photoexcitation, there are three distinct emission decay components, having decay times of 80 ps, 400 ps, and 2.4 ns.³² Polarization and spectral shift results, along with comparison to the known spectroscopy of bulk GaSe, allows assignment of the 80 ps transient to an electron relaxation. This relaxation was assigned to a direct to indirect band-edge transition, but concurrent electron trapping may occur as well. The subsequent 400 ps and 2.4 ns transients are assigned to hole trapping in shallow and deep traps, respectively. The extent of the spectral shifts associated with each of these components indicates that the trap depths are similar to those in the bulk material. Larger particles exhibit higher emission quantum yields and slower decays than smaller particles, indicating that trapping slows with increasing particle size. The conclusion that hole trapping occurs only relatively slowly will be important in the interpretation of the results presented here. Subsequent femtosecond studies, also

on 4 nm particles, detected transient absorption features in the 500–700 nm range. On the basis of the kinetics and carrier quenching studies, the absorption was assigned to hole intraband transitions.³³ In the initial studies, no assignment of the nature of the hole intraband transitions was made.

In this paper, we present a more detailed study of the transient absorption spectroscopy of GaSe nanoparticles. Much of the present study is made possible by further developments in nanoparticle synthesis. Specifically, we have developed methods by which relatively monodisperse samples may be synthesized, with particle diameters ranging from 4 to 9 nm. These nanoparticles are synthesized directly (without the use of subsequent chromatographic separation), ensuring that the surface chemistry is as size-independent as possible. We show that it is possible to control sizes and size distributions by continuing to grow small particles and focusing the size distribution. Detailed time-resolved absorption and absorption polarization measurements have been made on 4, 6, and 8 nm particles. These measurements, along with a simple, effective mass quantum confinement model allow assignment of the observed transient absorption spectrum. These assignments are consistent with the assignment that the transient absorption is dominated by hole intraband transitions, made on the basis on carrier quenching studies.

Experimental Section

Nanoparticle Synthesis and Characterization. Particles were synthesized by variations of the methods described earlier.³¹ 4-nanometer particles are synthesized as follows. A solution of 15 g of TOPO and 5 mL of TOP is heated to 150 °C overnight in nitrogen atmosphere. Prior to making this solution, the TOP (technical grade from Aldrich) is vacuum-distilled at 0.75 Torr, taking the fraction from 204 to 235 °C. A TOPSe solution made from 12.5 mL of TOP with 1.579 g of Se (99.999%) is then added to the mixture. The above TOP/TOPO/TOPSe reaction mixture is heated to 283 °C. This is followed by the injection of 0.8 mL of GaMe₃ dissolved in 7.5 mL of distilled TOP. Upon injection, the temperature drops 20–30 °C and then stabilizes at 280 °C. The reaction is allowed to proceed, with periodic withdrawal of small aliquots for monitoring the absorption spectrum. As soon as the absorption spectrum indicates that the particle size distribution is starting to broaden (evidenced by the absorption spectrum losing the sharpness of the onset), the sample is quickly cooled to room temperature. The synthesis takes about 40 min. The larger (6 and 9 nm) particles are synthesized in a similar way, except the reaction is initially allowed to proceed for 40 min. At this time, much smaller (0.2 mL) aliquots of the Me₃Ga solution are sequentially added. The smaller injections are repeated once every 2 min. This procedure is continued until the desired size is obtained. In the case of the 9 nm particles, this is done for about 40 min. The series of small injections results in a significant reactant concentration but not so high as to cause particle nucleation. Thus, this procedure results in particle growth and focusing of the particle size distribution. This type of procedure is well known, and similar procedures have been used to grow and focus the size distribution of CdSe nanoparticles.⁴⁰

Optical measurements are performed on these samples diluted in butanol. No effect was observed in the blanks or nanoparticle kinetics comparing reagent-grade butanol with that distilled over iodine-activated magnesium. The sample concentrations are set such that the absorbance in a 1 cm cell at the excitation wavelength (387.5 nm) is about 0.5. Increasing or reducing the concentration by a factor of 2 changes the magnitude of the observed transient absorptions but has no other discernible effect

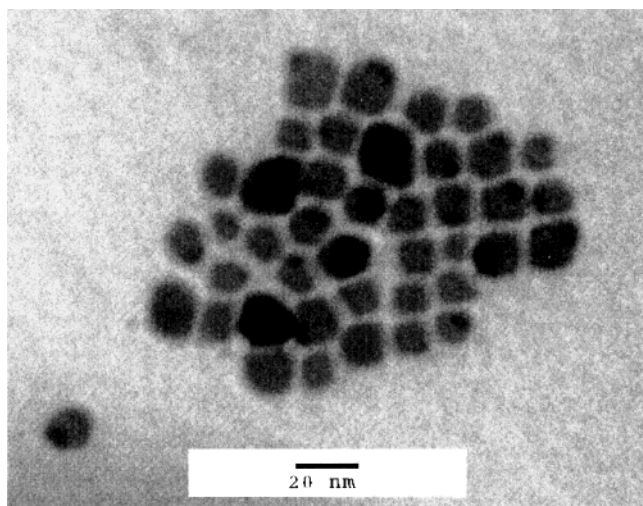


Figure 1. TEM images of 9 nm GaSe nanoparticles. Some particles appear larger and darker than others. This is probably due to stacking on the carbon grid.

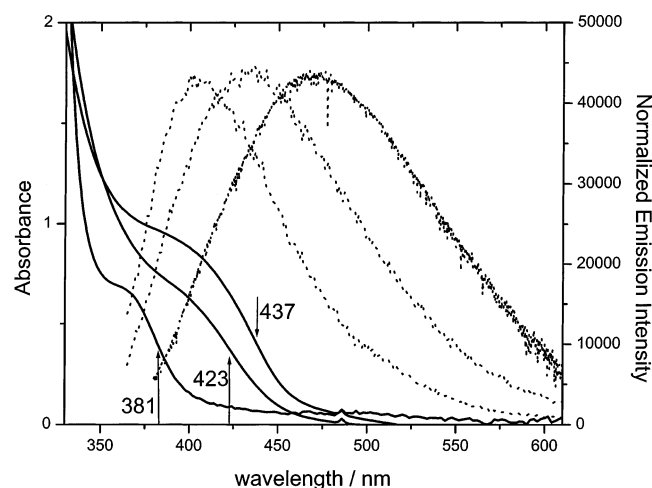


Figure 2. Absorption and emission spectra of 2.5, 4, and 9 nm nanoparticles. The absorption spectra have inflection points of 381, 423, and 437 nm, respectively. The emission spectra were obtained with 350 nm excitation.

on the transient absorption results. TEM images of the 2.5 and 4 nm particles have previously been published.³¹ A TEM image of the 9 nm particles is shown in Figure 1. Electron diffraction results on these particles are essentially identical to those reported previously for 4 nm particles. These results show that the particles consist of single Se–Ga–Ga–Se sheets. That is, the particles are exactly four atoms thick. These particles have an absorption onset that is to the red of that previously reported for smaller particles. The absorption and emission spectra of 2.5, 4, and 9 nm particles are collected in Figure 2. As discussed in a previous paper,³² the luminescence is a mixture of band-edge and trap-state emissions and therefore not as sharp as the absorption onsets. The figure also indicates the inflection points of the absorption onsets.

Optical Measurements. The transient absorption measurements were made on a femtosecond transient absorption polarization spectrometer. In this instrument, the femtosecond light source is a Clark-MXR CPM-2001, which produces 775 nm, 130 fs, 800 μ J pulses at a repetition rate of 1 kHz. About 4% of the pulse intensity is split off, attenuated, and used to generate a white light continuum that probes the sample. The low-intensity probe beam is split into reference and sample probe components. Wavelength selection is accomplished by use of

± 5 nm band-pass interference filters. The intensity of the probe pulses is much less than 1 μ J at the sample. The remainder of the 775 nm beam is doubled and attenuated to give ca. 1 μ J, 387.5 nm, 130 fs pulses at the sample. The pump beam is typically focused to a spot size of about 0.2–0.5 mm at the sample. The power density can be varied by changing the position of the sample with respect to the focal point of the pump beam. We find that below a specific power density, a decrease of the power density by a factor of 4 has no detectable effect on either the kinetics or the absorption anisotropies. Furthermore, an increase of the power density of a factor of 3 above this level has no discernible effect on the reconstructed spectra or the decay kinetics but slightly reduces the magnitude of the anisotropies. This is taken as an indication of the start of saturation effects at the higher power densities. The results presented here were obtained at power densities somewhat below the onset of detectable saturation effects.

Polarizations of the pump and probe beams are carefully controlled. Prior to the sample, in most experiments, the probe beam is linearly polarized at a 45° angle with respect to the (horizontal) polarization of the excitation pulse. This results in both transient dichroism and transient birefringence (optical Kerr effect) contributions to the observed signal.⁴¹ After the sample, the probe beam is split into horizontal and vertical polarization components. These beams and the I_0 beam are imaged onto UDT Sensors PIN 13DI photodiodes, biased at –15 V. The photodiode outputs are amplified and input into an Stanford Research Systems gated integrator. The gated integrator output is measured with a National Instruments 16-bit A/D converter in the data acquisition computer. The A/D converter and gated integrator triggering and reset are synchronized with the CPA-2001 Q-switch and controlled by home-built timing electronics. Data acquisition is controlled by LabView software running on a Pentium II computer.

With the apparatus in the 45° polarization configuration, the transient birefringence contribution to the signal dominates the observed kinetics at early times. To minimize the effect of the optical Kerr effect signals, some experiments were performed with the probe beam polarized parallel or perpendicular to the polarization of the pump pulses. From the combination of these two polarizations, time-resolved absorption anisotropies may also be determined. Comparison of the results obtained in the two different configurations (at 45° versus parallel and perpendicular polarizations) permits determination of the duration of the optical Kerr effect transient. This turns out to be about 5 ps for the samples studied here.

The emission spectra were obtained on a home-built fluorometer. Briefly, sample excitation is accomplished by a 150 W Xe–Hg lamp, followed by an Oriel 1/8 m double monochromator. The detection system consists of a 0.65 m ISA monochromator and a charge-coupled device (CCD) (Princeton Instruments Inc.). Emission spectra are not corrected for instrument response; however, the instrument response is fairly flat over the region of the study. Absorption spectra were obtained on a Hewlett-Packard 5486 diode-array spectrophotometer.

Results

The wavelength-dependent absorption kinetics of 8 nm GaSe nanoparticles are shown in Figure 3. These kinetics show an initial, approximately 5 ps transient. This feature is present in the butanol/TOP/TOPO blank with the apparatus in the 45° polarization configuration. The amplitude in the butanol/TOP/TOPO blanks is comparable to that observed in the nanoparticle

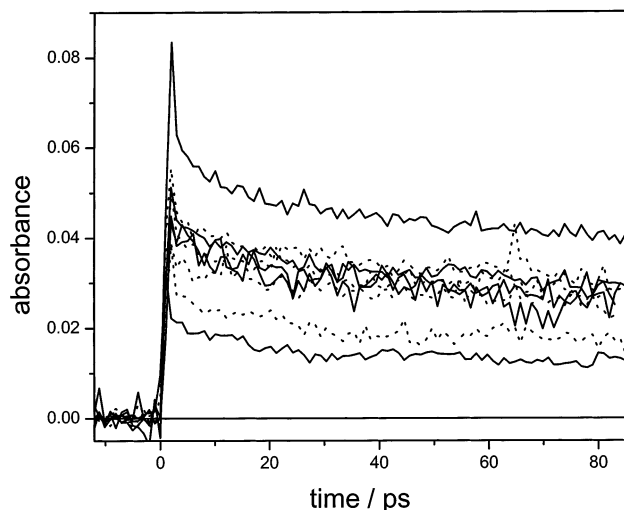


Figure 3. Transient absorption kinetics of 8 nm particles, observed at wavelengths between 540 and 700 nm. The wavelengths of the curves are (from most to least intense at 10 ps) 600, 620, 640, 660, 580, 680, 700, 560, and 540 nm. The 560, 620, 660, and 680 nm curves are dotted, and the others are solid.

samples. Higher time resolution scans show reproducible structure (oscillations) in the 0–5 ps kinetics. This short-lived transient is less intense in the 0° and 90° polarization configurations. These observations indicate that it is due to a four-wave mixing process in the solvent. The short-lived transient is unrelated to the nanoparticle electron and hole intraband spectroscopy and will not be discussed further.

Following the initial transient, there is a long-lived absorption due to the GaSe nanoparticles. This absorption has been assigned to intraband hole transitions, as previously reported.³³ This assignment was based on kinetics as well as hole quenching studies. In the present study, we focus on the assignment of the transitions giving rise to the observed absorption and evaluate the absorption spectral characteristics following relaxation of the initial, 5 ps transient. Figure 3 shows that the maximum absorption intensity is obtained at about 600 nm. The initial (integrated over the range of 10–30 ps) absorption intensities from the averages of several runs on the 4, 6, and 8 nm particles are collected to reconstruct the transient absorption spectrum in Figure 4. The figure shows that all three different particle sizes exhibit an absorption maximum at about 600 nm.

Assignment of the transitions giving rise to the observed absorption is facilitated by polarization measurements. The polarization of the transient absorption may be characterized by its anisotropy, defined as follows:^{42,43}

$$r = (A_{\text{par}} - A_{\text{perp}}) / (A_{\text{par}} + 2A_{\text{perp}}) = 1/5(3 \cos^2 \theta - 1) \quad (1)$$

where A_{par} and A_{perp} are the transient absorbances polarized parallel and perpendicular to the polarization of the excitation light. Equation 1 also relates the anisotropy to the angle between the excitation and transient absorption dipoles, θ . The excitation dipole is almost entirely z -axis polarized, both in bulk^{37,44} GaSe and in GaSe nanoparticles.³² Thus, a z -polarized transient absorption has $\theta = 0$ and results in an anisotropy close to 0.40. An x,y -polarized transient absorption has $\theta = 90^\circ$ and results in an anisotropy close to -0.20 . The wavelength-dependent absorption anisotropies are plotted in Figure 5. The figure shows that the absorption of each size of particle has a positive anisotropy near the absorption maximum of 600 nm and that the anisotropy is close to constant over the 600–700 nm range. The anisotropies decrease at bluer wavelengths for all particle

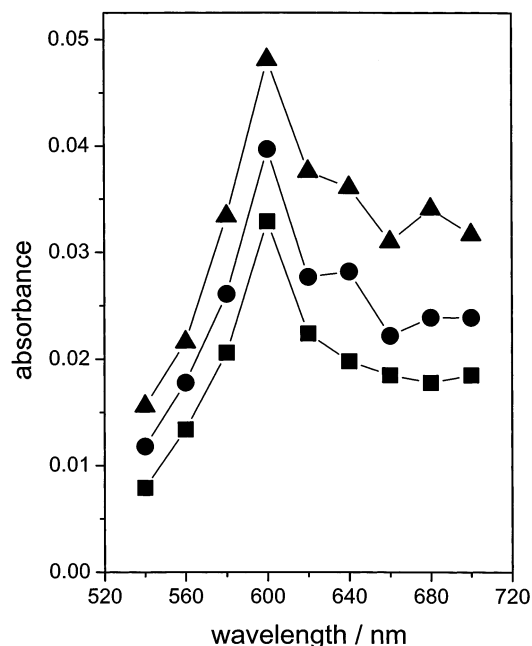


Figure 4. Plots of the unpolarized absorption (absorption parallel plus 2 times absorption perpendicular) intensities of 4 nm (■), 6 nm (●), and 8 nm (▲) nanoparticles, evaluated 20 ps following excitation.

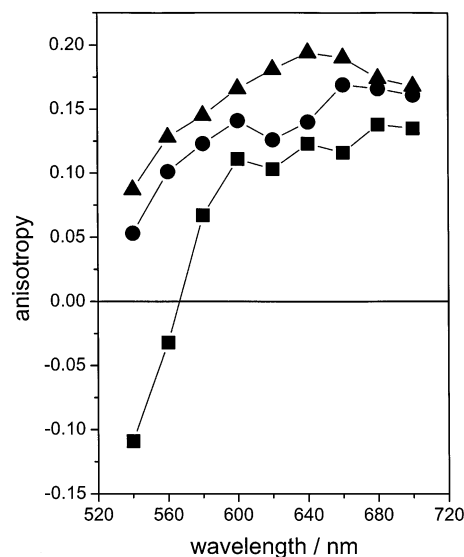


Figure 5. Plots of the absorption anisotropies of 4 nm (■), 6 nm (●), and 8 nm (▲) nanoparticles, evaluated 20 ps following excitation.

sizes, and the extent of this decrease depends on the particle size. A decrease of about 0.1 is observed for the 6 and 8 nm particles. In the case of 4 nm particles, a much larger decrease (about 0.24) is observed, with the anisotropy reaching about -0.12 at 540 nm. Despite the small transient absorbances at 540 nm, the trend of decreasing anisotropies with smaller particles is quite reproducible.

Figure 3 shows that the transient absorption exhibits significant decay on the 100 ps time scale. In a previous publication³³ we showed that hole trapping in 4 nm particles occurs on the 400 ps and 1.7 ns time scales. It is therefore reasonable to assign the transient absorption decay to hole trapping. Careful comparison of the decay curves in Figure 3, the decay curves for other particle sizes, and kinetic curves on which more decay is observed reveals that the kinetics are wavelength-independent. This observation is an important one, indicating that there is a single species giving rise to the entire absorption band. The

band may result from several different optical transitions, but this observation indicates that either the initial state for these transitions is the same or, if there is more than one initial state, they are all in a rapidly established thermal equilibrium. This observation therefore simplifies the possible spectroscopic assignments, discussed below. We note that a relatively weak transient absorption is also observed at bluer wavelengths, specifically 520 nm. However, the interpretation of the 520 nm results is more complicated than those observed at other wavelengths. GaSe nanoparticles are strongly emissive and the emission maximum is in the 500 nm region, with considerable emission occurring at 520 nm. Stimulated emission may therefore contribute to the observed 520 nm signal. The 520 nm decay kinetics provide evidence that both transient absorption and stimulated emission contribute to the observed signal, and these results are therefore not easily interpreted. We note that stimulated emission from semiconductor nanoparticles is an unusual and interesting phenomenon.^{45,46} We are currently studying this aspect of GaSe nanoparticle samples and the results will be published in a later paper.

The size independence of the observed (600 nm) absorption maximum might be taken as evidence that the absorption is due to trap-to-trap transitions. However, several observations indicate that such an assignment is incorrect, and the observed transient absorption must be assigned to intraband transitions. Emission polarization measurements clearly indicate that hole trapping occurs on the hundreds of picoseconds time scale in 4 nm GaSe nanoparticles.³² Somewhat slower trapping is observed in larger particles. Consistent with the slower hole trapping, we find that the emission quantum yield is larger in the larger (6–9 nm) particles. These observations indicate that very little trapping has occurred in the time frame (10–30 ps) at which the transient absorption spectrum is determined, establishing that an assignment to trap-to-trap transitions is incorrect. Furthermore, in light of the observation that trapping depolarizes the emission, we would expect for a trap-to-trap absorption to also be unpolarized. Figure 5 shows that this is not the case, also indicating that an assignment to trap absorption is untenable. We note that it might be argued that the observed absorption is too weak to be assigned to an intraband transition. However, these results were obtained at power densities below the onset of detectable saturation effects, and at these power levels, small absorbances from an intraband transition are expected.

Discussion

As mentioned above, kinetic and quenching results indicate that the transient absorption is primarily due to photogenerated holes. However, the spectroscopic results presented above cannot be understood simply in terms of the valence band structure of bulk GaSe. Band structure calculations and photoemission data indicate the presence of valence band states about 0.5 and 4.0 eV below the valence band edge.^{44,47} In contrast, the observed transient absorption peaks at 600 nm, about 2 eV. The conclusion is simple: bulk GaSe has no valence intraband transitions in this energy range. The observed transient absorption must therefore be assigned to transitions between quantum-confined hole states.

The simplest way to describe the electron and hole states is in terms of an effective mass model. This model is expected to qualitatively or semiquantitatively describe the spectroscopy of these states. It is an appropriate starting point for the description of these states in this relatively new, and thus far little-studied, nanoparticle system. Because of the disklike morphology of these particles, this model describes the electron and hole

energetics in terms of particle-in-a-cylinder energy levels. In cylindrical coordinates, the z - and x,y -dependence of the Schrodinger equation separate, and the wave function is written in terms of z -, r - [$= (x^2 + y^2)^{1/2}$], and ϕ - [$= \tan^{-1}(y/x)$] dependent functions. Specifically, for a cylinder of radius R and height H

$$\Psi(r, \phi, z) = N_{nm} J_m(a_{mn} r/R) \exp(im\phi) \sin(p\pi z/H) \quad (2)$$

where J_m is an m th-order Bessel function, a_{mn} is the n th root of a Bessel function of order m , N_{nm} is a normalization factor, and p is an integer. We have that⁴⁸

$$N_{nm} = (2/\pi H)^{1/2} (1/R) [1/J_{m+1}(a_{mn})]$$

The corresponding electron (hole) energy levels are

$$E_{m,n,p} = \frac{\hbar^2 a_{mn}^2}{2m_{e(h)}^{xy} R^2} + \frac{p^2 \hbar^2 \pi^2}{2m_{e(h)}^z H^2} \quad (3)$$

where $m_{e(h)}^{xy}$ and $m_{e(h)}^z$ are the electron (hole) effective masses in the x,y plane and along the z axis, respectively. At first sight, application of eq 3 seems completely straightforward: the particle dimensions (R and H) as well as the GaSe effective masses are known.^{37,49} For the indirect transition (in units of electron mass), $m_e^{xy} = 0.5$, $m_e^z = 1.6$, $m_h^{xy} = 0.8$, and $m_h^z = 0.2$. Calculation of the electron and hole energy levels from eq 3 has several limitations. An obvious problem is that the effective masses are known only to one significant figure accuracy. Another, more serious difficulty with this approach is that the effective mass as well as the rigid box (infinite potential) approximations break down as the particle size is decreased. These are reasonable approximations for the relatively large x,y dimensions of these disklike particles but are very poor approximations along the z axis, in which the particle extends for only four atoms, half of a unit cell. Much of the problem is that the wave function “spills out” of the cylinder along the z axis, with the net result being that the effective height of the cylinder, H_{eff} , is considerably greater than its geometric (crystallographic) height. Furthermore, there is no easy way to a priori calculate the value of H_{eff} . However, this problem is resolved by analysis of the size-dependent absorption spectra, Figure 2. The energy of the lowest (indirect band edge) transition is taken to be the inflection point of the spectrum, as indicated in Figure 2. The energy difference of the nanoparticle band edge and that of bulk GaSe is the quantum confinement energy and is simply the electron plus hole zero-point energies of eq 3. This energy is given by

$$E_0 = \frac{\hbar^2 a_{01}^2}{2R^2} \left(\frac{1}{m_e^{xy}} + \frac{1}{m_h^{xy}} \right) + \frac{\hbar^2 \pi^2}{2H_{\text{eff}}^2} \left(\frac{1}{m_e^z} + \frac{1}{m_h^z} \right) \quad (4)$$

a_{01} has a numerical value⁵⁰ of 2.405. Electron diffraction results show that all of the different sizes are a single tetralayer thick; they all have the same height, H_{eff} . Thus, a plot of the quantum confinement energy versus $1/R^2$ has an intercept of $(\hbar^2 \pi^2 / 2H_{\text{eff}}^2) \cdot (1/m_e^z + 1/m_h^z)$, which is a measure of the z -axis quantum confinement. This plot is shown in Figure 6. The intercept of this plot is 5640 cm^{-1} , which corresponds to the extent of z -axis quantum confinement of the lowest electron/hole state. We note that equating this value to the second term in eq 4 yields an H_{eff} value of 17.3 Å. This value has considerable uncertainty, due to the uncertainties in the effective masses. Despite these uncertainties, this value is considerably greater than the crystal-

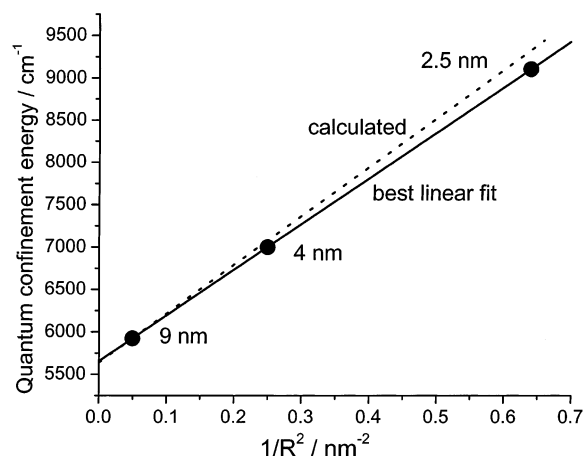


Figure 6. Plot of the quantum confinement energy (absorption inflection wavenumber – bulk absorption wavenumber) versus $1/R^2$. Also shown are a best linear fit through the data (—) and a line calculated from eq 4 (---).

lographic value of 7.95 Å. This result illustrates that due to the finite depth of the potential well, the wave function extends considerably past the ends of the potential well. We will return to this point later. Figure 6 also shows lines corresponding to the best linear fit through the data (slope = $5375 \text{ cm}^{-1}/\text{nm}^{-2}$) and a line having the same intercept and a slope calculated from eq 4, 5750 cm^{-1} . The figure shows that eq 4 slightly overpredicts the extent of x,y quantum confinement, which is typical of effective mass models. (We also note that Figure 6 may be used to easily determine the average nanoparticle diameter in any newly synthesized GaSe nanoparticle sample that displays a well-defined inflection point in the absorption spectrum.) It is important to note that the value of H_{eff} is not the parameter of interest in this calculation; it is simply the extent of z -axis quantum confinement, $(\hbar^2\pi^2/2H_{\text{eff}}^2)(1/m_e^z + 1/m_h^z) = 5640 \text{ cm}^{-1}$, and the effective masses that enter into the calculation of the electron and hole energy levels.

By use of the above value of $(\hbar^2\pi^2/2H_{\text{eff}}^2)(1/m_e^z + 1/m_h^z)$ and the known values of the z and x,y electron and hole effective masses, the electron and hole energy levels may be calculated from eq 3. With the assumed cylindrical ($D_{\infty h}$) symmetry, these states may be classified as g and u according to their inversion properties and as Σ , Π , Δ , etc., for $m = 0, 1, 2$, etc. The energy levels of these states are shown in Figures 7 and 8 for 4 and 6 nm particles, respectively. A crucial point is that the energies of the z -polarized transitions depend only on the thickness of the particle and the electron and hole effective masses; they are independent of the particle diameter. In contrast, the energies of the x,y -polarized transitions scale like $1/R^2$ and therefore are strongly dependent on the particle size. This difference is obvious in the comparisons of the Π manifolds of Figures 7 and 8. The calculated energies of the 8 nm particles (not shown) continue this trend, with the Π states being very closely spaced.

Dipole-allowed selection rules may be determined from the orthogonality relations of the Bessel and sine functions in eq 2. The selection rules are $\Delta m = 0, \Delta n = 0, \Delta p = \text{odd}$ (z -polarized) and $\Delta m = \pm 1, \Delta n = 0, 1, 2, \dots, \Delta p = 0$ (x,y -polarized). Note that with these selection rules, not all $g \rightarrow u$ transitions are allowed. Two types of allowed transitions from the lowest hole state are shown in Figures 7a and 8a: a single $\Sigma_g \rightarrow \Sigma_u$ (z -polarized) transition, and several $\Sigma_g \rightarrow \Pi_u$ (x,y -polarized) transitions. Similarly, Figures 7b and 8b show that two $\Sigma_g \rightarrow \Sigma_u$ (z -polarized) transitions and several $\Sigma_g \rightarrow \Pi_u$ (x,y -polarized) transitions are allowed. If electron/hole interactions, vibronic

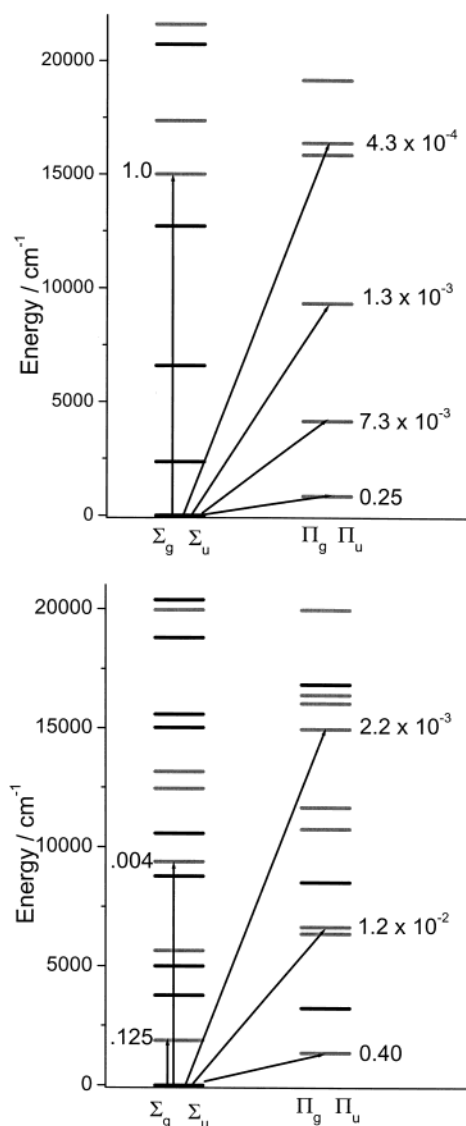


Figure 7. Hole (a, top panel) and electron (b, bottom panel) energy level diagrams calculated from eq 3 for 4 nm particles. The states having $m = 0$ and $m = 1$ are indicated as Σ and Π states, respectively. The g and u states are indicated in black and gray, respectively. Arrows indicate the allowed transitions from the ground state and their calculated relative intensities.

coupling, and environmentally induced symmetry breaking are ignored, then the integrated intensities of these transitions are simply proportional to the energy of the transition times the square of the transition dipole. The transition dipole integrals are easily evaluated and the relative intensities may therefore be calculated. These integrated absorption intensities from ground electron and hole levels are also given in Figures 7 and 8. As mentioned above, the energies of the x,y -polarized transitions are strongly dependent on the particle size. An important conclusion from this consideration is that, with a finite distribution of particle sizes, x,y -polarized electron and hole intraband transitions are expected throughout the visible region of the spectrum. Thus, a finite size distribution will result in a continuum of weak x,y -polarized absorption. Consideration of the electron and hole calculated relative intensities suggests that most of this continuum absorption may be assigned to electron transitions. The limitations of this model need to be understood: it is an effective mass model that considers the particles to be perfect cylinders at 0 K. These are pretty crude approximations. The transition energies and relative absorption intensities

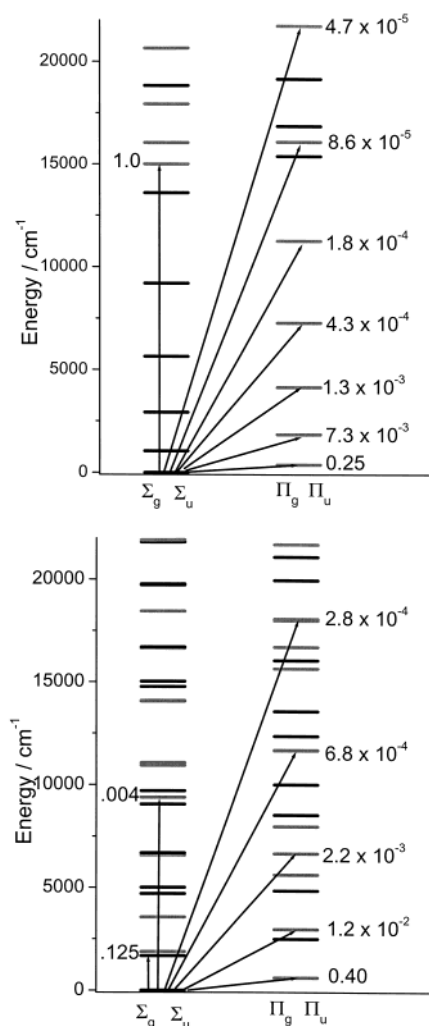


Figure 8. Same as Figure 7, except calculated for 6 nm particles.

ties calculated from this model are not expected to be quantitatively correct. However, the model permits classification of the states and allows qualitative and perhaps semiquantitative understanding of the intraband spectroscopy.

The conclusions from electron and hole intraband calculations with this simple model may be summarized as follows. There is an intense, z -polarized hole intraband absorption predicted at about $15\,000\text{ cm}^{-1}$ (667 nm). The wavelength of this absorption is independent of particle size. In addition, several much weaker x,y -polarized electron and hole transitions are predicted to produce an x,y -polarized continuum throughout the visible spectrum. The electron effective mass along the z axis is much greater than the corresponding hole effective mass ($1.6m_e$ versus $0.2m_e$). Thus, the z -polarized electron intraband transitions occur at a much lower energy than in the hole case and there are no strong electron intraband transitions calculated in the red and near-IR spectral regions, only a moderately weak z -polarized ($p = 1 \rightarrow p = 4$) transition in the near IR. The net effect is that an absorption maximum is predicted in the red region of the spectrum (667 nm), and near this maximum, the absorption is predicted to be largely z -polarized. To the blue of this maximum, there are only weaker, x,y -polarized absorptions. To the red of this maximum there are very weak x,y -polarized electron and hole transitions and a moderately weak z -polarized electron transition. These predictions are in agreement with the results shown in Figure 4. The figure shows an absorbance maximum at about 600 nm, close to the predicted value of 667 nm. We note that the electron and hole effective masses are

not precisely known and that uncertainties in these values could easily explain the differences between the observed and calculated absorption maxima.

The absorption anisotropy spectra in Figure 5 provide a more stringent test of the above assignments. There are several obvious features of these spectra. First, independent of particle size, the anisotropies in the 600–700 nm range are approximately constant and positive. The anisotropies decrease at wavelengths shorter than 600 nm. Second, the larger particles exhibit more positive anisotropies than do the smaller particles over the entire spectrum. Third, the differences between the small and large particle anisotropy spectra are largest at the furthest blue wavelengths. The particle-size-dependent absorption polarizations predicted from Figures 7 and 8 are also in qualitative or semiquantitative agreement with these experimental results, as discussed below.

The model predicts a positive anisotropy at the absorption maximum, where the absorption is dominated by the intense, z -polarized $\Sigma_g \rightarrow \Sigma_u$ hole transition. For the other transitions to give a significant contribution to the observed absorption, they must be more intense than these calculations indicate. However, significant approximations are made in this simple treatment. In particular, electron/hole interactions will mix the electron and hole z -polarized transitions, increasing the intensity of the calculated near-infrared ($p = 1 \rightarrow p = 4$) electron transition. Since these nanoparticles are about the same size as the exciton in bulk GaSe, significant electron/hole interactions are expected. To the red of the 600 nm absorption maximum, there are the very weak x,y -polarized electron and hole transitions and the moderately weak, z -polarized $p = 1 \rightarrow p = 4$ electron transition. We suggest that the hole and electron $\Sigma_g \rightarrow \Sigma_u$ transitions dominate the red part of the spectrum, resulting in the observed positive anisotropy in the 600–700 nm region.

As stated above, this treatment ignores vibronic coupling (phonon interactions) and environmental symmetry breaking. Phonons and environmental effects that break the cylindrical symmetry mix Σ and Π states, giving additional intensity to the $\Sigma_g \rightarrow \Pi_u$ transitions. With this consideration in mind, the model also rationalizes the decrease in anisotropy on the blue edges of the spectrum, where we suggest that the absorbance is primarily due to the underlying $\Sigma_g \rightarrow \Pi_u$, x,y -polarized continuum. The model also rationalizes the observation that the x,y -polarized contribution to the absorption is greatest for the smallest particles. Figures 7 and 8 show that the calculated intensities of the $\Sigma_g \rightarrow \Pi_u$ transitions decrease with increasing energy. This is because, with increasing n , the Bessel functions are more oscillatory and therefore have less overlap with the lowest energy wave function, $J_0(a_{01}r/R)$. Equation 3 indicates that the states of smaller particles are shifted to higher energies, with the result being that states with smaller values of n contribute to the blue absorption. Thus, Figures 7 and 8 show that more intense x,y absorption and hence smaller anisotropy is predicted for smaller particles. Figure 5 shows that this prediction is in accord with the experimental results.

None of the polarizations are as large as would be predicted from purely z - and x,y -polarized oscillators. However, the above calculations also ignore spin–orbit coupling, which mixes z - and x,y -polarized transitions in bulk GaSe.³⁷ The overlapping z - and weaker x,y -polarized transitions in Figure 7 along with the effect of spin–orbit coupling results in an absorbance that is less than completely z -polarized near the absorption maximum. We conclude that this simple model facilitates the assignments of the observed transient absorption but can only qualitatively explain the features of the anisotropy spectrum.

As discussed above, the initial assignment of this absorption to (dominantly) hole intraband transitions was based on the transient absorption kinetics obtained in pyridine,³³ and this assignment is confirmed by comparison with the results of the simple model presented above. Pyridine is known to act as a hole acceptor,⁵ and as previously reported,³³ this absorption is significantly quenched for the 4 nm particles. We note that this quenching is less complete in larger particles and the largest particles undergo very little quenching. This observation rationalizes the seemingly discordant observation that in pyridine solution the emission is not as effectively quenched as the transient absorption. All samples have a finite particle size distribution, and the transient absorption result indicates that the smallest particles within the distribution are most effectively quenched. Our previous studies have shown that the largest particles are most strongly luminescent.³² The holes in the largest, most luminescent particles are not effectively quenched in pyridine solution, consistent with both sets of observations. The reason for this is easily understood in terms of the simple model discussed above. The redox potential of the valence band varies with the particle size, shifting to more positive potentials in the smaller particles. Within the framework of the above model, the amount of this shift (compared to the valence band of bulk GaSe) is given by

$$E_{\text{vb}} = \frac{\hbar^2 a_{01}^2}{2m_{\text{h}}^{\text{xy}} R^2} + \frac{\hbar^2 \pi^2}{2m_{\text{h}}^{\text{z}} H_{\text{eff}}^2}$$

Thus, hole transfer to an adsorbed acceptor is most energetically favorable in the smallest particles.

It is of interest to compare the intraband spectroscopy of GaSe nanoparticles to that in CdSe and InP nanoparticles. In the latter cases, the observed absorptions are in the infrared (0.2–0.5 eV) and are assigned to 1S → 1P electron intraband transitions. We note that relaxation of the 1P level occurs on the time scale of a fraction of a picosecond to a few picoseconds in those cases.^{7,8} In contrast, the most intense transition observed in the GaSe case is assigned to a hole transition at approximately 15 000 cm⁻¹. It would be of interest to compare the CdSe and InP relaxation rates with the analogous $p = 2$ to $p = 1$ hole relaxation rates in these nanoparticles. We are in the process of measuring these dynamics, and those results will be reported in a later paper.

Finally, we return to the point that the electron and hole wave functions extend well past the top and bottom surfaces of these disklike nanoparticles. Our view of these nanoparticles is that the TOP/TOPO passivating ligands are attached to the gallium atoms at the nanoparticle edges and that the selenium surfaces are coordinatively saturated and therefore chemically inert. Thus, the accessibility of the electron and hole charge densities is a characteristic of the two-dimensional nature of these nanoparticles along with the effective masses. Having the charge density extend well past the passivating surface layer occurs very little in three-dimensional nanoparticles. The presence of charge density extending past the van der Waals surfaces can result in strong coupling to other species on the particle surface. For example, this results in strongly interacting nanoparticle aggregates, analogous to “*J*-aggregates” in organic molecules.⁵¹ This type of aggregation effect is very unusual among semiconductor nanoparticles.^{52–55} In addition, the large spatial extent of the electron and hole wave functions can result in extremely facile interfacial charge transfer. The spectroscopy of GaSe aggregates is currently being studied, and the results will be reported in later papers.

Conclusions

Several conclusions may be drawn from the results presented here:

1. It is possible to focus the size distributions of GaSe nanoparticles to obtain relatively monodisperse samples, with diameters ranging from 4 to 9 nm.
2. A transient absorption throughout the visible and near-infrared is observed for all particle sizes and is assigned to hole intraband transitions.
3. The absorption maximum occurs at about 600 nm, independent of particle size. This absorption is largely *z*-polarized near the 600 nm maximum and largely *x,y*-polarized at wavelengths considerably to the blue of the maximum. In the smallest particles, this absorption is largely quenched in pyridine, indicating that it is dominated by hole intraband transitions.
4. The wavelength and size independence of the absorption maximum as well as the anisotropy spectrum may be understood in terms of an effective mass model. In this model, the energies and intensities of the *z*- and *x,y*-polarized electron and hole intraband transitions are calculated from particle-in-a-cylinder wave functions. This simple model correctly predicts that the absorption is dominated by a *z*-polarized hole transition and semiquantitatively predicts the wavelength of the absorption maximum. It also gives qualitative agreement with the observed anisotropy results.

Acknowledgment. This work was supported by a grant from the Department of Energy, Grant DE-FG03-00ER15037.

References and Notes

- (1) Kamat, P. V.; Meisel, D., Eds. *Semiconductor Nanoclusters—Physical, Chemical and Catalytic Aspects*; Elsevier: Amsterdam, 1997.
- (2) Guyot-Sionnest, P.; Hines, M. A. *Appl. Phys. Lett.* **1998**, *72*, 686.
- (3) Shim, M.; Shilov, S. V.; Braiman, M. S.; Guyot-Sionnest, P. *J. Chem. Phys. B* **2000**, *104*, 1494.
- (4) Shim, M.; Wang, C.; Guyot-Sionnest, P. *J. Phys. Chem. B* **2001**, *105*, 2369.
- (5) Burda, C.; Link, S.; Mohamed, M.; El-Sayed, M. A. *J. Phys. Chem. B* **2001**, *105*, 12286.
- (6) Klimov, V. I.; Schwarz, C. J.; McBranch, D. W.; Leatherdale, C. A.; Bawendi, M. G. *Phys. Rev. B* **1999**, *60*, R2177.
- (7) Klimov, V. I.; McBranch, D. W. *Phys. Rev. Lett.* **1998**, *80*, 4028.
- (8) Blackburn, J. L.; Ellingson, R. J.; Micic, O. I.; Nozik, A. J. *J. Phys. Chem. B* **2003**, *107*, 102.
- (9) Eychemüller, A.; Hässelbarth, A.; Katsikas, L.; Weller, H. *Ber. Bunsen-Ges. Phys. Chem.* **1991**, *95*, 79.
- (10) Skinner, D. E.; Colombo, D. P., Jr.; Cavaleri, J. J.; Bowman, R. M. *J. Phys. Chem.* **1995**, *99*, 7853.
- (11) Zhang, J. Z.; O’Neil, R. H.; Roberti, T. W. *J. Phys. Chem.* **1994**, *98*, 3859.
- (12) Zhang, J. Z.; O’Neil, R. H.; Roberti, T. W.; McGowen, J. L.; Evans, J. E. *Chem. Phys. Lett.* **1994**, *218*, 479.
- (13) Kim, S. H.; Wolters, R. H.; Heath, J. R. *J. Chem. Phys.* **1996**, *105*, 7957.
- (14) Micic, O. I.; Cheong, H. M.; Fu, H.; Zunger, A.; Sprague, J. R.; Mascarenhas, A.; Nozik, A. J. *J. Phys. Chem. B* **1997**, *101*, 4904.
- (15) Langof, L.; Ehrenfreund, E.; Lifshitz, E.; Micic, O. I.; Nozik, A. J. *J. Phys. Chem. B* **2002**, *106*, 1606.
- (16) Wehrenberg, B. L.; Wang, C.; Guyot-Sionnest, P. *J. Phys. Chem. B* **2002**, *106*, 10634.
- (17) Cavaleri, J. J.; Colombo, D. P., Jr.; Bowman, R. M. *J. Phys. Chem. B* **1998**, *102*, 1341.
- (18) Cherepy, N. J.; Liston, D. B.; Lovejoy, J. A.; Deng, H.; Zhang, J. Z. *J. Chem. Phys. B* **1998**, *102*, 770.
- (19) Sengupta, A.; Jiang, B.; Mandal, K. C.; Zhang, J. Z. *J. Phys. Chem. B* **1999**, *103*, 3128.
- (20) Zhang, J. Z. *J. Phys. Chem. B* **2000**, *104*, 7239.
- (21) Kelley, D. F. In *Semiconductor Photochemistry and Photophysics*; Ramamurthy, V., Schanze, K. S., Eds.; Marcel Dekker: New York, 2003; Vol. 10, p 173.
- (22) Chikan, V.; Kelley, D. F. *J. Phys. Chem. B* **2002**, *106*, 3794.

- (23) Doolen, R.; Laitinen, R.; Parsapour, F.; Kelley, D. F. *J. Phys. Chem. B* **1998**, *102*, 3906.
- (24) Huang, J. M.; Kelley, D. F. *J. Chem. Phys.* **2000**, *113*, 793.
- (25) Huang, J. M.; Laitinen, R.; Kelley, D. F. *Phys. Rev. B* **2000**, *62*, 10995.
- (26) Chikan, V.; Waterland, M. R.; Huang, J. M.; Kelley, D. F. *J. Chem. Phys.* **2000**, *113*, 5448.
- (27) Woggon, U.; Geissen, H.; Gindele, F.; Wind, O.; Fluegel, B.; Peyghambarian, N. *Phys. Rev. B* **1996**, *54*, 17681.
- (28) Klimov, V. I.; Mikhailovsky, A. A.; McBranch, D. W.; Leatherdale, C. A.; Bawendi, M. G. *Phys. Rev. B* **2000**, *61*, R13349.
- (29) Guyot-Sionnest, P.; Shim, M.; Matranga, C.; Hines, M. *Phys. Rev. B* **1999**, *60*, R2181.
- (30) Underwood, D. F.; Kippeny, T.; Rosenthal, S. J. *J. Phys. Chem. B* **2001**, *105*, 436.
- (31) Chikan, V.; Kelley, D. F. *Nano Lett.* **2002**, *2*, 141.
- (32) Chikan, V.; Kelley, D. F. *J. Chem. Phys.* **2002**, *117*, 8944.
- (33) Chikan, V.; Kelley, D. F. *Nano Lett.* **2002**, *2*, 1015.
- (34) Levy, F. *Crystallography and Crystal Chemistry of Materials with Layered Structures*; Reidel: Dordrecht, The Netherlands, 1976.
- (35) Grasso, V. *Electronic structure and electronic transitions in layered materials*; Reidel: Dordrecht, The Netherlands, 1986.
- (36) Wieting, T. J.; Schluter, M. *Electrons and Phonons in Layered Crystal Structures*; Reidel: Dordrecht, The Netherlands, 1979; Vol. 3.
- (37) Mooser, E.; Schluter, M. *Nuovo Cimento* **1973**, *18B*, 164.
- (38) Capozzi, V. *Phys. Rev. B* **1989**, *40*, 3182.
- (39) Murray, C. B.; Norris, D. J.; Bawendi, M. G. *J. Am. Chem. Soc.* **1993**, *115*, 8706.
- (40) Peng, X.; Wickham, J.; Alivisatos, A. P. *J. Am. Chem. Soc.* **1998**, *120*, 5343.
- (41) Fleming, G. R. *Chemical Applications of Ultrafast Spectroscopy*; Oxford: New York, 1986.
- (42) Albrecht, A. *J. Mol. Spectrosc.* **1961**, *6*, 84.
- (43) Tao, T. *Biopolymers* **1969**, *8*, 609.
- (44) Schluter, M. *Nuovo Cimento* **1973**, *13B*, 313.
- (45) Klimov, V. I.; Mikhailovsky, A. A.; Xu, S.; Malko, A.; Hollingsworth, J. A.; Leatherdale, C. A.; Eisler, H.-J.; Bawendi, M. G. *Science* **2000**, *290*, 314.
- (46) Mikhailovsky, A. A.; Malko, A.; Hollingsworth, J. A.; Bawendi, M. G.; Klimov, V. I. *App. Phys. Lett.* **2002**, *80*, 2380.
- (47) Camara, M. O. D.; Mauger, A.; Devos, I. *Phys. Rev. B* **2002**, *65*, 125206.
- (48) Arfken, G. *Mathematical Methods for Physicists*; Academic Press: New York, 1970.
- (49) Ottaviani, G.; Canali, C.; Nava, F.; Schmid, P.; Mooser, E.; Minder, R.; Zschokke, I. *Solid State Commun.* **1974**, *14*, 933.
- (50) Abromowitz, M.; Stegun, I. A., Eds. *Handbook of Mathematical Functions*; Dover: New York, 1965.
- (51) Davydov, A. S. *Theory of molecular excitons*; Plenum: New York, 1971.
- (52) Kagan, C. R.; Murray, C. B.; Bawendi, M. G. *Phys. Rev. B* **1996**, *54*, 8633.
- (53) Micic, O. I.; Jones, K. M.; Cahill, A.; Nozik, A. J. *J. Phys. Chem. B* **1998**, *102*, 9791.
- (54) Dollefeld, H.; Weller, H.; Eychmuller, A. *Nano Lett.* **2001**, *1*, 267.
- (55) Dollefeld, H.; Weller, H.; Eychmuller, A. *J. Phys. Chem. B* **2002**, *106*, 5604.